Continuous-Slice PENN-PET: A Positron Tomograph with Volume Imaging Capability

Joel S. Karp, Gerd Muehllehner, David A. Mankoff, Caesar E. Ordonez*, John M. Ollinger†, Margaret E. Daube-Witherspoon‡, Arthur T. Haigh, and Daniel J. Beerbohm

Department of Radiology, University of Pennsylvania, Philadelphia, Pennsylvania

The PENN-PET scanner consists of six hexagonally arranged position-sensitive NaI(Tl) detectors. This design offers high spatial resolution in all three dimensions, high sampling density along all three axes without scanner motion, a large axial acceptance angle, good energy resolution, and good timing resolution. This results in three-dimensional imaging capability with high sensitivity and low scatter and random backgrounds. The spatial resolution is 5.5 mm (FWHM) in all directions near the center. The true sensitivity, for a brain-sized object, is a maximum of 85 kcps/μCi/ml and the scatter fraction is a minimum of 10%, both depending on the lower level energy threshold. The scanner can handle up to 5 mCi in the field of view, at which point the randoms equal the true coincidences and the detectors reach their count rate limit. We have so far acquired [^{18}F]FDG brain studies and cardiac studies, which show the applicability of our scanner for both brain and whole-body imaging. With the results to date, we feel that this design results in a simple yet high performance scanner which is applicable to many types of static and dynamic clinical studies.

J Nucl Med 1990; 31:617–627

High spatial resolution in a positron tomograph with the capability of simultaneously imaging multiple slices can be achieved by some form of position encoding to avoid the complexity resulting from individual photomultiplier tubes (PMT) coupled to individual small crystals. We have recently completed a continuous-slice positron emission tomograph (PET) using six large-area sodium iodide (NaI(Tl)) crystals coupled to 50-mm square PMTs, which results in a large number of resolution elements with relatively few detectors compared to other approaches. The design and per-

formance of this instrument, which is based on a previously constructed single-slice version (*1*), is described in this paper, emphasizing those aspects which differ from other designs.

The PENN-PET scanner was designed with the following intentions:

1. To develop an alternative approach to the multi-crystal/PMT, multi-ring, BGO systems.
2. To achieve the best possible performance.
3. To explore the advantages of volume imaging.
4. To produce a clinically useful instrument at a reasonable price.

The idea for the PENN-PET scanner was conceived in the early 1980s, at a time when the best transverse spatial resolution of PET scanners was 10 mm and the axial resolution was 15 mm. The quest for better image resolution led many groups to using smaller BGO crystals coupled one-to-one to small PMTs (*2,3*) and then to position encoding schemes, with as many as eight-crystals/PMT (*4,5*). These configurations have led to a transverse resolution for multi-slice scanners of ~5 mm, and an axial resolution as low as 6 mm, by reducing the height of the crystal and adding more rings. The PENN-PET detectors, on the other hand, use a high degree of position encoding, 100 resolution elements per PMT, so that a large transverse and axial field of view (FOV) is continuously sampled at high resolution in a relatively simple fashion. The spatial resolution and countrate capability have been improved by modifying the detectors, rather than by making them smaller.

The use of continuous NaI(Tl) detectors results in several desirable features. The scanner has good spatial resolution in all three dimensions which, combined with high sampling density along all three axes, allows the data to be organized into transverse, coronal, sagittal or oblique views without incrementally moving the patient or interpolating between slices. The system achieves good spatial sampling through the use of continuous detectors and therefore does not require detector motion such as wobbling or rotation, the absence of which is particularly useful in gated cardiac imaging and fast dynamic scans. The system uses a relatively

large acceptance angle in the axial direction, relying on shielding only to reduce the amount of scattered radiation, not to define the slices in the axial direction. NaI(Tl) has good energy resolution, which allows for an effective rejection of scattered events. NaI(Tl) also has good timing resolution, which allows the use of a relatively narrow coincidence resolving time window, thereby reducing the background due to random coincidence events. Finally, since the system uses only six scintillation crystals and 180 PMTs as compared to thousands of crystals and PMTs in other designs, the system is relatively simple in design.

While our approach has several inherent advantages, the use of continuous detectors in PET also has limitations. The gaps between the detectors result in missing data and require special compensation in the reconstruction algorithm to reduce the loss of image quality. In addition, the use of only a few large detectors results in high countrates in each detector, which requires special hardware and software techniques to achieve a high overall system countrate capability. Finally, NaI(Tl) has lower sensitivity than other scintillation crystals used in PET, however, the large axial acceptance angle helps compensate for this loss.

DESIGN OVERVIEW

The continuous-slice PENN-PET positron tomograph (Fig. 1) uses a hexagonal arrangement of six position-sensitive NaI(TI) detectors (6). The detector separation is 84 cm and the patient port is restricted to a 50-cm diameter through lead shielding, which also limits the axial field of view to 10 cm. Each detector consists of a 500×150×25 mm NaI(Tl) scintillator with a 12.5-mm thick glass light guide coupled to the back surface. The scintillation light is detected by an array of thirty 50-mm square PMTs, arranged in three rows of ten. The high light output of NaI(Tl), necessary for

FIGURE 1
Continuous-slice PENN-PET scanner in the Hospital of the University of Pennsylvania.

good spatial resolution, allows the use of delay-line pulse-clipping of the exponential tails of the NaI(Tl) light emission, as well as relatively short pulse integration times in order to minimize the effects of pulse pileup. The pulses from each PMT are amplified and fed into a digitizer/integrator. A dedicated hardware position calculator determines the positions along both axes from the integrated signals, using a biased centroid calculation (7). This calculation can include all 30 PMTs to calculate a global centroid or it can be restricted to ~10 PMTs in the vicinity of the scintillation site for a local centroid calculation. At high count rates, the local centroid calculation has the advantage that nearly simultaneous events in the crystal have a reduced effect on the estimated position.

Following position estimation, the detector locations, along with detector pair, energy and timing information, are sent to a rebinning pre-processor, based upon an earlier design (8), which reorganizes the data into 50 projection matrices (256 rays × 192 angles per matrix), which are called sinograms.

The sinograms undergo the following stages of processing.

1. Normalization, to correct for nonuniformities in sensitivity.
2. Background subtraction, to correct for scatter, randoms, and other misplaced events.
3. Attenuation correction.
4. Gap compensation, to correct for the missing data in the gaps between detectors, that result from both the physical gap between detectors and the difficulty of positioning near the edge of the detector. (In the sinogram, the gaps appear as diagonal lines separating the detector pairs.)

Finally, transverse section images are reconstructed by filtered backprojection. The slice thickness and spacing of the transverse images can be varied in 2-mm increments, depending on the study, and they can be reorganized into coronal and sagittal images, also with variable slice thickness.

The next section discusses the detectors and data processing in more detail, particularly those areas unique to this scanner.

SYSTEM HIGHLIGHTS

Detectors

Spatial resolution. The spatial resolution depends largely on the extent to which the scintillation light spreads in the crystal after a gamma ray interaction as well as the extent of the gamma ray energy spread by Compton scattering. Both light and energy spread are reduced in a thinner crystal, although the lower sensitivity would preclude its use in PET. It is possible, however, to manipulate the spread of light in a given crystal thickness which affects noise propagation due to the statistical fluctuations of the PMT signals and, therefore,

influences the spatial resolution (9). To decrease light spreading, shallow grooves were cut into the front surface of the crystal (forming columns and rows of pyramids) to reflect light back towards the PMTs with less dispersion. Secondly, a rectangular array of 50-mm square PMTs was chosen to optimize the sampling of the light while minimizing the total number of PMTs needed for each detector. Finally, the effective light spread was changed by varying the bias in the positioning algorithm to the point where only nine to eleven PMTs contribute significantly to the calculated position. This improves the resolution by eliminating small noisy signals originating from PMTs far from the scintillation site.

In the transverse direction the spatial resolution is an average of 5.2 mm at the full-width at half-maximum (FWHM), and 13 mm at the full-width at tenth-maximum (FWTM). The point spread function (PSF) is more peaked than a Gaussian and has tails that are somewhat wider, due to Compton scattering in the crystal. The spatial resolution degrades very close to the edge of the crystal, since a centroid calculation can not effectively position events at this point. Events near the edge of the crystal are therefore rejected, resulting in an active length of 450 mm. The gap corresponds to ~10% of the length of the detector, resulting in a 20% loss of data in the transverse plane. In the axial direction, the average spatial resolution is 6.2 mm FWHM and the active length is 90 mm, which determines the effective axial field of view (FOV).

Calibration. In a continuous detector, the PMT gain calibration and position calibration are essential for good peformance. PMT gain calibration is performed in software and results in good energy uniformity over the detector with a standard deviation (s.d.) in peak energy of only 1% and an energy resolution of 10%. However, even with perfectly balanced gains, the position is only approximately linear because of systematic variations due to nonuniform light collection and sampling, and nonlinearities in the biased centroid calculation. Therefore, spatial distortions are measured and compensated. A sealed calibration source consisting of 31 individual ^{68}Ge/^{68}Ga sources spaced 15 mm apart is placed between each pair of parallel detectors. Lead masks in front of the detectors, with seven rows of holes angled to point towards the line of sources, collimate the gamma rays towards known detector locations. The effects of background scattering and collimator penetration are minimized through the use of a position-dependent coincidence requirement. The resulting 217 peaks (31 × 7), in the two-dimensional position spectrum are identified in each detector, and since the distortions vary slowly between measured points, linear interpolation between the peaks is used to obtain distortions at 0.5-mm increments in both directions. A look-up table of spatial distortion corrections is created so that measured positions can be converted to true positions during data collection. The PMT gain calibration is normally performed only approximately four times per year, and the spatial calibration is normally performed monthly, to account for electronic drift.

High Count Rates. The performance of the detectors at high count rates is limited by three problems: (a) dead time, (b) pulse pile-up, and (c) random coincidences. Detector deadtime and pulse pile-up have been examined extensively (10). By clipping the NaI(Tl) light response (to 120 ns), using a short integration time (160–240 ns), and by using a local centroid calculation (11), it has been possible to achieve

detector single rates of 2 million cps per detector, corresponding to a system-wide true coincidence rate of 100 kcps. At this rate, detector deadtime is at most 20%, while the spatial resolution FWHM increases by 20% and the FWTM increases by 50%.

The high count rate performance of any system of detectors designed for PET is ultimately limited by the occurrence of random coincidences. The relative rate of random coincidences to true coincidences is given by:

$$R/T = 2\tau n_c N_s^2 / k n_s N_s \sim 2\tau N_s / k, \qquad (1)$$

where N_s is the singles rate per detector, 2τ is the coincidence timing window, n_c is the number of detector pairs, n_s is the number of detectors, and k is the true coincidence fraction. R/T, the random fraction, can be minimized either by increasing k, the fraction of events found in coincidence, or by decreasing 2τ. The fraction k is affected by the lower level energy discriminator, choice of detector material, scanner geometry and shielding. The narrowness of the coincidence window is limited by the detector's timing resolution. Between two two-dimensional detectors, we measure 3.8 ns FWHM and 8.2 ns FWTM. The timing coincidence window, 2τ, is set to 8 ns, which includes up to 95% of the coincidences.

Sinogram Data Processing

Normalization. The first correction applied to the two-dimensional sinograms is normalization. There are three effects that need to be normalized. The first is the axial sensitivity variation from the edge of the axial FOV to the center, where the sensitivity is peaked. The second is the sampling pattern which results from the coordinate transformation and truncation in going from the detector coordinates (1,024 channels in the transverse direction) to the sinogram coordinates (256 rays × 192 angles). These two effects do not change with time. The third effect, which does change with time, results from nonuniformities in the detector which remain after energy and spatial calibrations. This detector normalization is done biweekly in order to minimize errors in both image quality and quantitation.

We normalize each of nine detector pairs by taking data with a uniform sheet source of low activity placed sequentially between each detector pair. The data are processed in a manner similar to that proposed by Casey et al. (12). Rather than determining the normalization for up to 1 million (1,024 channels × 1,024 channels) possible coincidences in each detector pair for each slice, which requires an unreasonable number of total counts to minimize statistical noise, the normalization is calculated for each sinogram coordinate, which reduces the number of coincidence locations by a factor of ~128. If we assume that the individual efficiency for each detector channel is independent of the opposing detector channel with which it is in coincidence, then the normalization can be determined by averaging the detector over all coincidences with the opposing detector. In other words, the normalization factor for each sinogram coordinate is given by:

$$N(s,\theta) = \sum n_a(s_i,\theta_j) \sum n_b(s_k,\theta_l) / \sum n(s_m,\theta_p), \qquad (2)$$

where n_a is the number of counts in the sinogram for a given position in detector a and summed over all coincident positions in detector b. These coincidences fall along a line in the sinogram for the given detector pair, defined by $\theta_j = C s_i + D$,

which passes through the point (s, θ) and is parallel to the lines which correspond to the gaps adjacent to detector a. The counts represented by n_b are defined similarly. The sum over n includes all counts in the detector pair. This further reduces the number of counts needed by about a factor of 64. Therefore, this averaging process of each sinogram coordinate reduces the number of counts needed for good statistics by about a factor of 10^4, compared to normalizing each detector coincidence.

Background Subtraction. The second correction applied to the sinogram is background subtraction. This includes scattered and other misplaced events. The background profile was determined for brain studies by using a brain-sized phantom uniformly filled with activity except for a thin region in the middle. The phantom is a lucite cylinder 18-cm in diameter by 10-cm long, with a 2.5-cm wide polyethylene bar in the middle, which has nearly the same density as water. The profile of this distribution, at an angle along the direction of the bar, shows a dip in the middle and tails at the edges, which should go to zero in the absence of background events (see

Scatter Phantom

CHANNEL
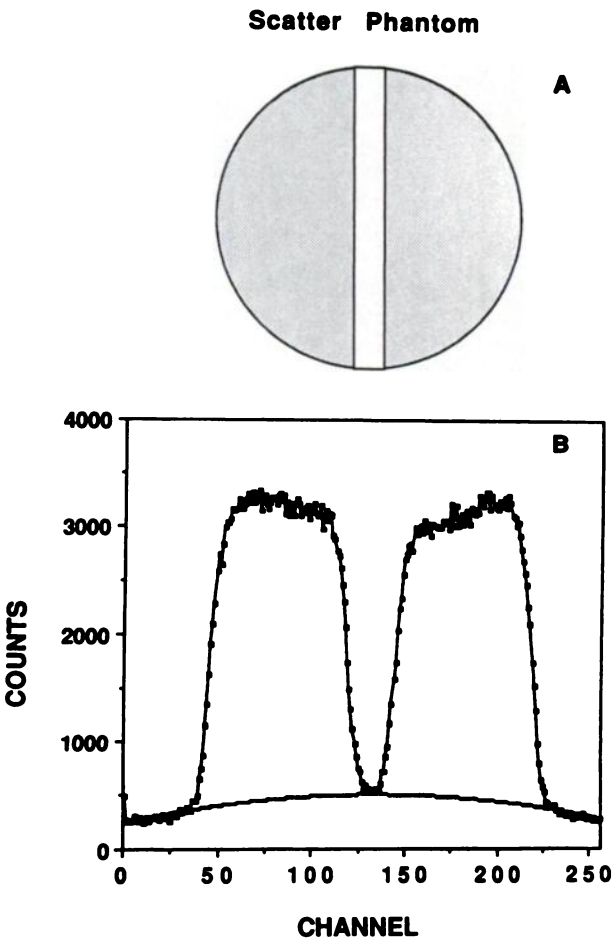
FIGURE 2
(A) Scatter phantom is 18 cm in diameter by 10 cm long. A 2.5-cm polyethylene bar in the middle creates a region free from activity. (B) Profile of the phantom in the sinogram at an angle along the direction of the bar. The data are not corrected for attenuation. The background is fit to the tails, outside the phantom, and the center dip. The data were taken at a very low countrate.

Fig. 2). This parabolic scatter profile is assumed to be valid for brain studies, so that the total background in the FOV in the sinogram can be estimated by measuring the background in the tails at the edge of the distribution as a function of angle. The background is calculated for each sinogram and is then subtracted from the data. This subtraction technique, while only approximate, improves the contrast of the image and allows quantitative measurements to be made. Compared to scatter subtraction by deconvolution, this method is advantageous in that it takes into account scattered radiation from areas outside the sinogram being processed. The background subtraction includes randoms, which, for a typical fluorine-18-fluorodeoxyglucose ($[^{18}F]$FDG) brain study, is only $\sim 5\%$.

Attenuation Correction. This is presently accomplished by fitting the skull or body with an elliptical outline and calculating the attenuation using the known coefficient for water while a transmission scanning source is implemented.

Image Reconstruction and Gap Compensation. For most scanners, the axial acceptance angle is usually small, since the slices are determined by septa between rings. Our system is continuous in the axial direction, without slice-defining septa, and therefore has a potentially large axial acceptance angle. For a source in the center of the scanner, the maximum angular acceptance $\alpha_{max} = 6.5°$ (as measured from the central transverse plane). This large acceptance angle yields an increase in sensitivity, but if the data are processed into parallel slices, it also causes a degradation in the spatial resolution as the radial distance from the center of the scanner increases. Figure 3 illustrates the trade-off between sensitivity and axial resolution. For the point in the center, the calculated $Z_{avg} = (Z_1 + Z_2)/2$ is the same Z_{true}, even for large α. However, for the points off-center, the difference between Z_{avg} and Z_{true} increases as α increases, leading to poorer axial resolution for large α. For example, a point 10 cm off-center in the transverse plane can be mispositioned up to 1 cm in the axial direction.

The degradation in spatial resolution as a function of radius can be minimized by limiting the angular acceptance angle, at the expense of sensitivity. Alternatively, we can use a three-

Axial Profile
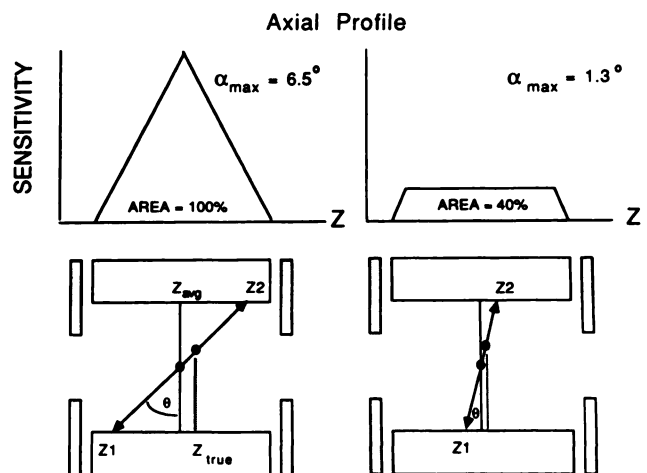
FIGURE 3
(A) Axial acceptance angle $\alpha_{max} = 6.5°$ maximizes both the sensitivity and the error in the axial position Z for points which are off-center in the transverse direction. (B) $\alpha_{max} = 1.3°$ reduces the sensitivity to 40% and the error in Z by approximately a factor of five.

dimensional method of reconstruction which does not require shift-invariance of the PSF, such as the event-by-event back-projection (EBEBP) technique (13). This algorithm backprojects the data into a three-dimensional volume, taking the axial angle into account. This technique reduces the resolution degradation without reducing the sensitivity. The backprojected data can then be reconstructed with the iterative space reconstruction algorithm (ISRA) (14), since this algorithm operates on the backprojected volume rather than the projection data. Before reconstruction, however, the volume is sliced into parallel transverse images, which are then independently reconstructed. Both the EBEBP and ISRA are time-consuming (on a VAX 11/750) and would require special hardware to make them practical. However, a three-dimensional reconstruction algorithm would optimize the performance of the PENN-PET scanner.

The method normally used for image reconstruction is filtered backprojection with the constrained Fourier space technique to compensate for the gaps. This method for estimating the missing data is iterative and is based on properties of the two-dimensional Fourier transform of the sinogram (15). We have also evaluated other algorithms, including the ISRA, which can compensate for the missing data (16); however, they offer no advantage in accuracy with patient data, and have considerably longer reconstruction time. The constrained Fourier technique transforms the current estimate from one space to the other in an alternating sequence, imposing the known constraints in the respective spaces. We take the two-dimensional Fourier transform of the sinogram,

$$P(\omega,\eta) = \int_\theta \int_s p(s,\theta) \exp[-i(\omega s + \eta\theta)] \, ds \, d\theta, \quad (3)$$

where the coordinates in the Fourier domain are spatial frequency ω and harmonic number η. This has been shown (17), for a point source:

$$|P(\omega,\eta)| = J_\eta(\omega R),$$

where $J\eta$ is the η_{th} order Bessel function, implying that in Fourier space valid data are essentially confined to the "wedge" region for which $\eta \le \omega R_o$, where R_o is the object radius. Because the detector gap corresponds to a radius R_g which is larger than the radius R_o, in Fourier space the data gaps result in coefficients which are inconsistent with valid data. A complete projection set, without gaps, then, produces a Fourier transform with coefficients of nonnegligible amplitude only inside the wedge for which $\eta \le R_o$, while the Fourier transform of the incomplete projection data contains nonnegligible coefficients outside this wedge. If these coefficients outside the wedge are set to zero, an inverse Fourier transform of the remaining coefficients yields a consistent estimate of a complete set of projection data. Since all the data are modified in the process, we insert only the estimated gap data into the original sinogram rather than using the complete inverse Fourier transform. Also, since the gaps are not completely separable in Fourier space, the estimate of the gap data can be improved by iterating this procedure several times. Since it involves mainly forward and inverse Fourier transforms, the technique lends itself well to implementation on an array processor.

Figure 4A shows the sinogram matrix of a simulated Hoff-
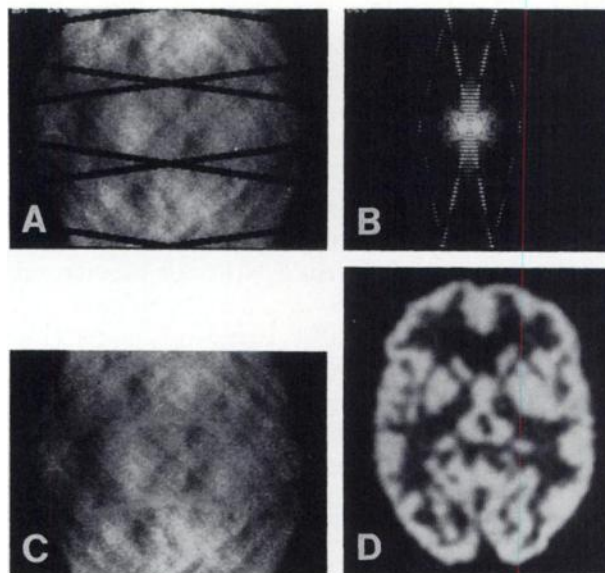
FIGURE 4

(A) Sinogram matrix of simulated brain phantom with gaps, with 5-mm (FWHM) detector resolution. (B) Fourier transform of phantom with gaps. (C) Sinogram matrix which results after three iterations of the constrained Fourier space gap compensation method. (D) Reconstructed image (of C) using filtered backprojection.

man phantom with data gaps, appearing as diagonal bars of missing data. Approximately 20% of the projection data are lost as a result of inserting the gaps. The Fourier transform in Figure 4B has distinct diagonal lines due to the gaps superimposed on the wedge of real data. The Fourier components in the forbidden region are set to zero, and then the inverse transform is taken, resulting in a sinogram with estimated data in the gaps. Only the estimated gap data are inserted into the original projection matrix (Fig. 4A) so as not to smooth the real data. Figure 4C shows the result after three iterations. Estimated data in the gaps in Fig. 4C are barely noticeable, since the major structures in the sinogram continue in a consistent manner across the gaps. An image reconstructed from this sinogram, Figure 4D, is nearly indistinguishable from one which is reconstructed from the simulated sinogram without gaps.

SYSTEM PERFORMANCE

Spatial Resolution

The coincidence resolution midway between two detectors is given by the convolution of the PSFs of two detectors. In the PET scanner, gamma rays can strike the crystal at an oblique angle, leading to a parallax error, since the depth of interaction is unknown. This effect is noticeable in the transverse direction and causes the image spatial resolution to degrade somewhat in the transverse plane as the distance from the center increases, but only minimally affects the axial resolution because of the relatively smaller angles of incidence allowed in that direction. In addition, with the PENN-PET scanner, as with others, the spatial resolution depends on many factors, such as radial and axial

position, axial collimation, and reconstruction algorithm. Therefore, we have measured the intrinsic spatial resolution of the scanner and its dependence on a variety of scanner parameters, to indicate expected image quality under different scanning conditions.

Since the PENN-PET has continuous sampling and good resolution in all three directions, it was necessary to use a true point source to measure the transverse and axial resolutions simultaneously. The point source was a 1-mm³ piece of copper, irradiated by protons in a cyclotron to form a ^{62}Zn/^{62}Cu positron emitter (150 μCi) with a 9.2-hr half-life. The source was inserted in plastic tubing for handling and positioned at a number of locations throughout the FOV of the scanner in order to measure the dependence on radial and axial positions. With the point sources, the dependence of the spatial resolution on axial acceptance angle and reconstruction algorithm was studied. We have evaluated the spatial resolution using the full angular acceptance α_{max} = 6.5° and also 1.3°. As seen in Figure 3, sensitivity decreases by a factor of 2.5 while the maximum axial positioning error decreases by about a factor of five with the decreased axial acceptance angle. The magnitude of that error depends upon the radial distance of the source from the center. The data were reconstructed two-dimensionally, namely filtered backprojection (using a ramp filter) after rebinning, and three-dimensionally, using the EBEBP and ISRA algorithms. Since the transverse resolution of a point source is a function of the number of iterations with the ISRA algorithm, the data were reconstructed for a fixed number of iterations (four) to show the relative changes of the resolution, both transversely and axially, as a function of radius.

The measured spatial resolution, as characterized by the FWHM, as a function of position, is shown in Figure 5. The data were collected with sufficient statistics so that a reliable determination of the FWHM could be made from the PSF by linear interpolation between adjacent channels. The image PSF is more sharply peaked than a Gaussian, and one which needs to be finely sampled (channel width less than FWHM/10) in order to properly measure the spatial resolution. Using a large axial acceptance angle, the two-dimensional approach to reconstruction results in the axial resolution increasing from 5.5 to 10.5 mm at a radius of 15 cm (Fig. 5A). The transverse resolution also increases, although less dramatically, in a direction perpendicular to the direction in which the source is moved. This results from reconstructing an inconsistent set of projection data, since data at angles parallel to the direction in which the source is moved are misplaced axially into other slices because of the two-dimensional approximation. The effect of this approximation is less noticeable with patient data, which normally are reconstructed into slices thicker than 2 mm. The radial
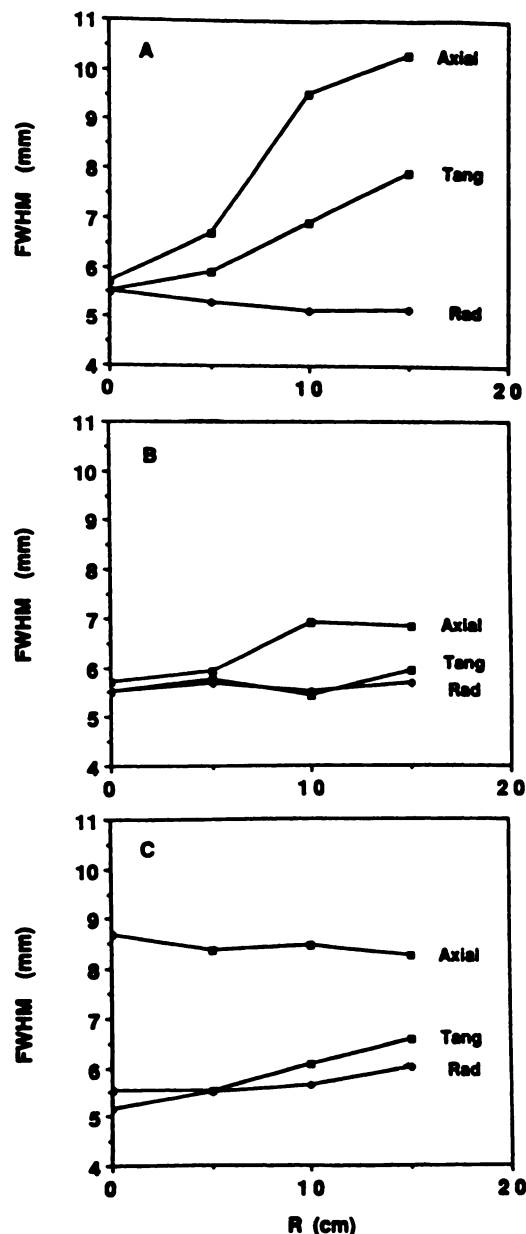
FIGURE 5
Image spatial resolution, in the transverse plane (X and Y) and the axial direction (Z) with the axial acceptance angle α_{max} = 6.5° with the data processed by parallel slice rebinning. (B) α_{max} = 1.3° with parallel slice rebinning. (C) α_{max} = 6.5° with the data processed by event-by-event backprojection.

smearing of the PSF which normally occurs with a circular scanner is not seen, since with the hexagonal PENN-PET, the effect of the depth-of-interaction is less sensitive to the location of the source. The degradation in both the axial and transverse resolution as a function of radius is minimized by using a small axial acceptance angle (Fig. 5B). The three-dimensional reconstruction technique, however, which backprojects each event in a volume, nearly eliminates the degradation in resolution with radius (Fig. 5C) without reducing the sensitivity. Since the volume data were sliced into transverse

planes and reconstructed two-dimensionally, rather than using a true three-dimensional reconstruction algorithm with appropriate filtering, the resolution in the axial direction is not optimal in Figure 5C.

Scatter and Sensitivity

One of the features that sets the continuous-slice PENN-PET scanner apart from most other systems is the fact that there are no septa between rings. Septa are normally used to define slice, limit the axial acceptance angle, and limit the amount of scattered radiation. With continuous detectors slice definition with septa is not necessary or even desirable, and because of the good energy resolution of NaI(Tl) and energy uniformity of the detectors, energy discrimination rather than shielding effectively limits scatter. The flexibility of adjusting the energy threshold (in both hardware and software) and the axial acceptance angle (only in software) allows us to study the trade-off between scatter and sensitivity and to alter the parameters depending on the type of study. To estimate the amount of scattered radiation for brain studies and its dependence on acceptance angle and energy threshold, we used a brain-sized cylindrical lucite phantom (18-cm diameter × 10-cm long) filled with a small amount of ^{18}F. Figure 2 shows the activity profile, with a polyethylene bar in the middle as described earlier, and the parabolic fit to the background, which we assume to be the scatter profile over the region covered by the phantom. The scatter fraction is defined as the ratio of the scattered coincidences, within the region of activity, to true coincidences. Thus, with the bar in the phantom, the scatter fraction can be estimated by comparing the average amplitude of the background to the average amplitude of the trues, within the region of the phantom. This method is a convenient means of comparing the scatter fraction for different energy thresholds and axial acceptance angles. For comparison, we calculated the scatter fraction for our system using the method suggested by Hoffman (18). This method deduces the scatter fraction for each annular ring of the cylinder from the tails in the PSF of a line source placed at several positions in the uniform water-filled phantom, and then integrates over the rings for the total scatter fraction of the cylinder. The two methods give the same result for a given energy threshold and axial acceptance angle.

Figure 6 shows coincidence energy spectra taken with a point source in air (lower curve) and with the water-filled scatter phantom (upper curve). The singles energy spectra show much more scatter at low energies for the phantom compared to a point source in air, but, in the coincidence spectra, most large-angle scattering events are eliminated by the coincidence requirement. Since the singles photopeak efficiency in NaI(Tl) is only approximately two-thirds of the total interaction efficiency, which is 60% for a 2.5-cm thick crystal, there are many events which Compton scatter out of the
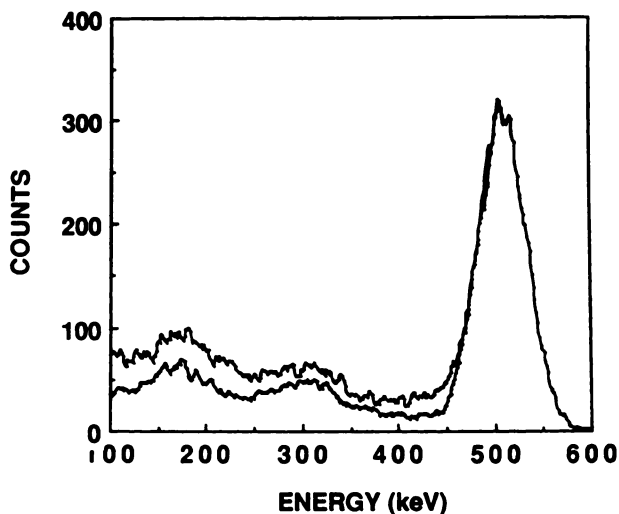
FIGURE 6
Energy spectra for a point source in air (lower curve) and for a water-filled 18-cm diameter phantom (upper curve).

crystal and are "good" in the sense that the measured position is correct even though the measured energy is lower than 511 keV. These "good" events, however, have the same energy as "bad" events in which Compton scatter in the patient is detected at positions inconsistent with the original trajectory. Therefore, as the energy threshold is raised, good (true) events as well as bad (scatter) events are eliminated. In other words, the true sensitivity will decrease at the same time that the scatter fraction (specifically, scatter in the patient) decreases.

Figure 7 shows that with the largest axial opening, the scatter fraction ranges from a high of 40% with a lower level energy discriminator (LLED) set at 100 keV to a low of 10% with the LLED set to 500 keV, which
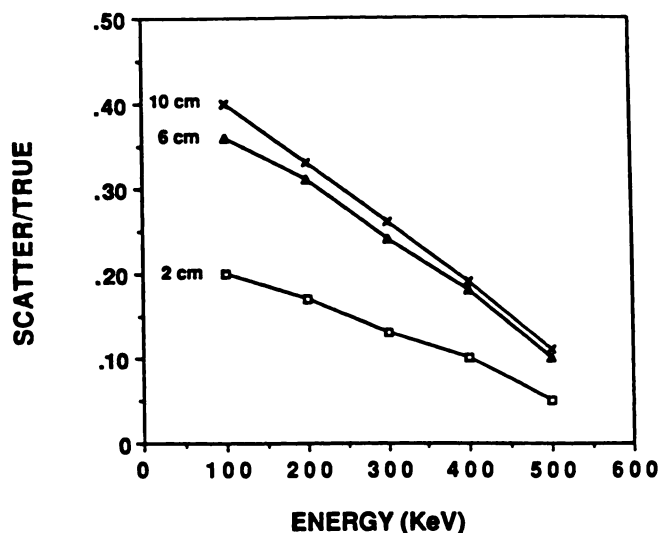
FIGURE 7
Scatter fraction (scatter/true) versus lower level energy threshold (LLED) and axial opening (10 cm, 6 cm, 2 cm).

overlaps the photopeak because of the finite energy resolution. Because of the finite energy resolution, some scattered events have measured energies in the photopeak range, so that even with the highest energy threshold there is still a non-negligible scatter fraction. Figure 8 shows the dependence of the sensitivity on the LLED, as expressed in the standard units of Kcps/μCi/ml. The true sensitivity is a maximum of 85 Kcps/μCi/ml with the LLED = 100 keV, or an average of 9.5 Kcps/μCi/ml/axial-cm over the entire axial FOV. The latter value is comparable to multi-ring systems, which usually quote the sensitivity for direct and cross slices of ~1-cm axial thickness. However, note that the phantom used to measure sensitivity (with the polyethylene bar taken out) is 18 cm in diameter by 10 cm, which closely approximates the volume of the brain. Also, the sensitivity represents only the true counts, after subtraction of both randoms and scattered events, which fall in the region of the brain-sized phantom and not in the entire FOV. The sensitivity drops by more than a factor of two as the LLED is raised from 100 keV to 400 keV, while the value of the scatter fraction also drops by a factor of two; thus raising the energy threshold trades better contrast for fewer true counts.

A previous comparison of the scatter (and random) fraction and sensitivity for NaI(Tl) (and BGO) was performed (19) as a function of energy threshold with a pair of small detectors. For NaI(Tl), which has a lower photofraction than BGO, the lowest threshold (100 keV) was concluded to give the best image quality, based on using an image quality factor Q = T/(S/T + R/T + 1), where T is the number of true, S the number of scatter, and R the number of random coincidences. For the present tomograph, we studied the effect of the energy threshold on image quality (20), by measuring the signal-to-noise ratio (SNR) of cold spheres in a uniformly filled cylinder of water with ^{18}F. The SNR is the ratio of the contrast of the cold spheres to the relative background noise. With a real scanner, the background noise includes a nonstatistical component (e.g., detector nonuniformities, reconstruction artifacts) as well as a statistical component, whereas the previous study using only a pair of detectors assumed the ideal condition of having only statistical noise. Unlike the previous study, the optimal SNR, for spheres ranging from 1 cm to 2.5 cm diameter, is achieved with a high (400 keV) threshold for typical count densities, since the decrease in true counts with a high threshold does not offset the increase in contrast. For low count densities, where statistical fluctuations dominate the background noise, a lower threshold results in comparable image quality to use of a higher threshold.

In order to compare the effectiveness of limiting scatter by energy discrimination versus axial angular discrimination, we measured the scatter fraction as a function of axial angular acceptance. Changing the acceptance angle in software does not affect the scatter

fraction. This is because the scatter and true coincidences have the same triangular axial sensitivity response. Note that the phantom used is only 10 cm long, since in a clinical situation, the activity in the body is a fair distance away and, therefore, effectively shielded from the detectors. Scattering investigations by others have generally assumed an axially continuous distribution of activity extending beyond the bounds of the scanner. To better understand the consequence of having no inter-slice septa, the shielding was physically moved to change the axial opening from the normal 10 cm to 2 cm. Figure 7 shows that for a 20-percent scatter fraction, one can either use a 2-cm axial opening with the LLED = 100 keV, or a 10-cm axial opening with the LLED = 400 keV. Both of these possibilities result in similar true sensitivities, since the sensitivity changes by about a factor of two in going from 400 keV to 100 keV and by a factor of two and a half in going from a 10-cm to 2-cm axial opening (see Fig. 8). Also, the scatter fraction does not change significantly when the aperture is increased from 6 cm to 10 cm (Fig. 7), although this may depend on the phantom used. Therefore, with sodium iodide, energy discrimination can be used to reduce the scatter fraction with a smaller cost to sensitivity than would result with mechanical collimation. In addition, limiting the angular acceptance with inter-slice septa precludes continuous axial sampling and good axial resolution with a stationary system. Two recent studies (21,22) have investigated the effect of varying the axial acceptance angle using Monte Carlo simulations, both showing a significant increase in the scatter fraction with large acceptance angles. However, these simulations were performed for brain-only BGO scanners, which have both a smaller detector diameter than the body-sized PENN-PET and poorer energy resolution.
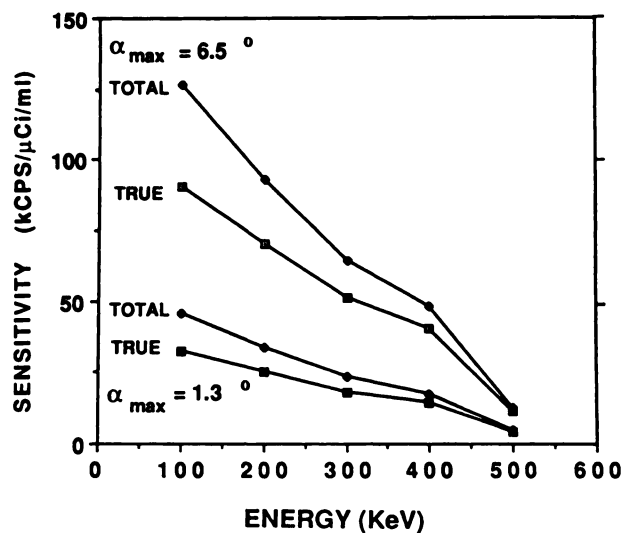
FIGURE 8
Sensitivity versus lower level energy threshold for total (true + scatter) coincidences and trues, for α_{max} = 6.5° and 1.3°. The values are for the 18 cm diameter by 10 cm long phantom.

Count Rate Performance

The two major adverse consequences of operating the system at high count rates are random coincidences and deadtime. To measure the behavior of the system as a function of activity, we filled the 18-cm cylindrical phantom with a high activity of ^{18}F and measured the total, true, and random coincidence rates within the region of the phantom. Results for a fixed LLED = 350 keV are shown in Figure 9. The total coincidences that affect the image are calculated from the total input rate times the fraction of coincidences that fall within the area of the object. Since we have only nine pairs of detectors, the total coincidence input rate is easily measured. The randoms affecting the image are calculated as:

$$R = 2\tau \; n_c \; N_s^2 \; F_s,$$

where 2τ is the coincidence timing window set at 8 ns, n_c is the number of detector pairs, N_s is the singles rate per detector, and F_s is the fraction of randoms which fall within the area of the object.

The coincidence timing and triggering electronics experience small deadtime losses at the highest count-rates. At the present time, the majority of the deadtime loss occurs in the event-processing electronics, namely the position calculator and rebinning pre-processor. With an activity of ~3.5 mCi, the position calculator throughput saturates at a rate of 180 Kcps for the local centroid calculation, typically using only 10 PMTs, and 125 kcps for the global centroid calculation, which uses all 30 PMTs. Hardware modifications which will sig-

nificantly increase the maximum countrate of the system are currently under development.
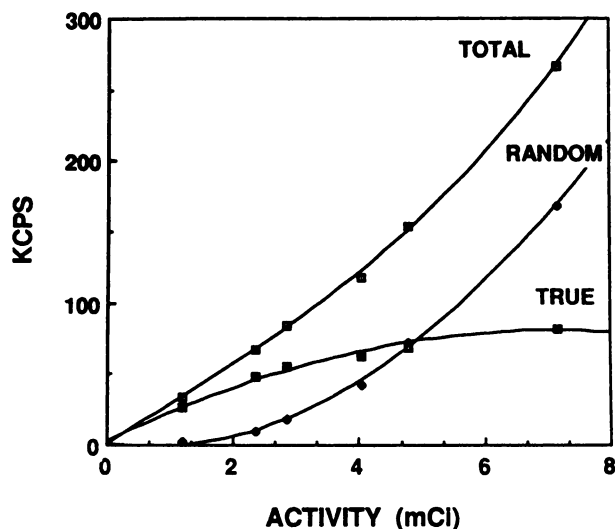
The true rates are calculated by subtracting the random and scatter rates from the total coincidences. The scatter/true ratio is 20% for LLED = 350 keV. At this energy threshold, the trues equal the randoms with an activity in the FOV of 4.5 mCi, at which point the true coincidence rate is 80 Kcps. With photopeak energy discrimination, including lower and upper level energy thresholds, the true coincidence countrate is somewhat lower. With the global centroid, simultaneous events pile up and register an energy above 511 keV, which need to be rejected since the calculated position will most likely be wrong. The local centroid reduces the pile-up of simultaneous events to a large extent.

With or without photopeak energy discrimination, the local centroid algorithm leads to fewer positioning errors at high countrates than the global centroid algorithm. This is shown in Figure 10, which plots the ratio of the background to true counts in the bar phantom profile. At low count rates, the background fraction is simply the scatter fraction. At higher count rates, the background fraction is comparable to the scatter plus random fractions. Up to 3 mCi in the FOV, the local centroid, without a photopeak window, provides as low a background fraction and almost double the true event rate as the global centroid with a photopeak window. An even lower background fraction, however, can be obtained at these count rates using the local centroid with a photopeak window, with a commensurate reduction in true event rate.

For a typical [18F]FDG brain study, a maximum of 1 mCi is in the FOV, which leads to a true count rate

FIGURE 9
Count rate versus activity in the region of the phantom at LLED = 350 keV. Shown are the randoms, trues, and total coincidences (true + randoms + scatter) as measured by the system, using a local centroid positioning algorithm without an upper level energy discriminator.
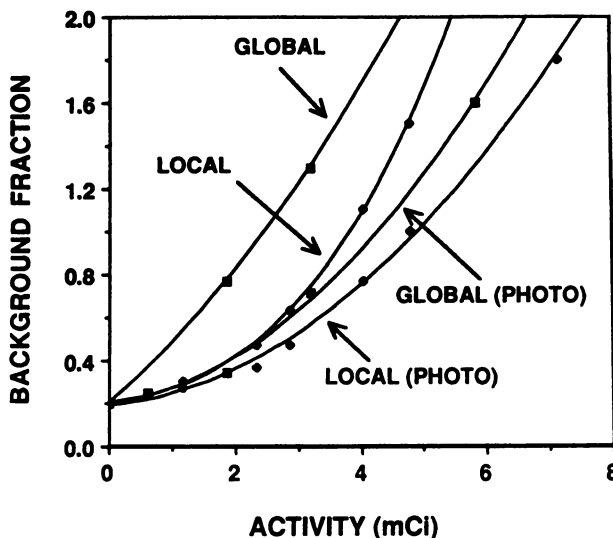
FIGURE 10
Background fraction (scatter fraction + random fraction) versus activity, as characterized by the ratio of "cold" region to "hot" region in the bar profile phantom.

of 20 Kcps (above 350 keV), or ~35 million counts for a 30-min scan, with a combined (scatter + random) background fraction of 25% and minimal deadtime losses. At higher data rates, detector performance has a significant effect on image quality. A previous study (23) has shown that high count rate image quality is optimized when the high count rate event processing techniques were implemented. The detectors have been shown to perform well above 2 Mcps corresponding to 4–5 mCi in the FOV, at which point random and true rates are approximately equal.

Clinical Images

To date, mainly [18F]FDG brain studies have been performed. A typical study is shown in Figure 11. The patient was injected with 4.8 mCi and scanned for 50 min, beginning 40 min postinjection. Typically, patients are injected with 4–8 mCi and scanned for 30–50 min. The data are sorted into as many as 45 transverse sections, each 2 mm thick. Figure 11 shows representative transverse sections that are 6-mm thick and separated by 4 mm. The good spatial resolution and sampling in the axial direction are evident when the data are sorted into sagittal or coronal slices (see Fig. 12). A cardiac scan, displayed in Figure 13, was obtained with a 12-min acquisition, 30 min after an 8-mCi [18F]FDG injection.

DISCUSSION

The continuous NaI(Tl) detectors used in the PENN-PET scanner result in 5.5-mm resolution in both the
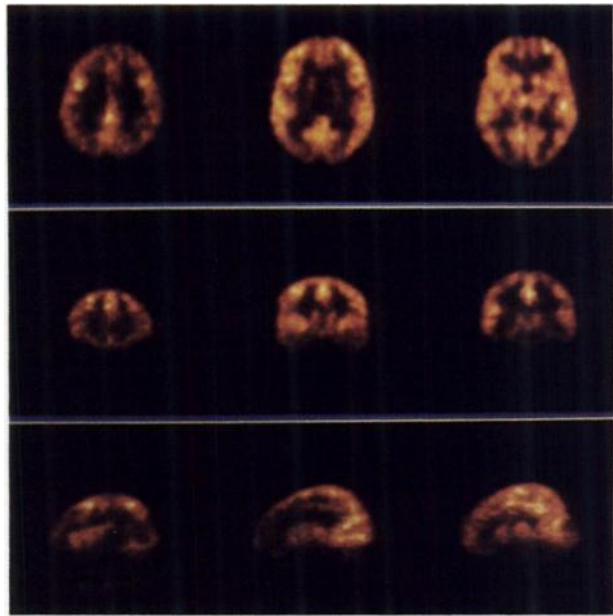
FIGURE 12
Representative transverse, coronal, and sagittal sections, 6 mm thick, of [18F]FDG brain study. The patient was scanned at two axial positions, in order to get complete coronal and sagittal images with good statistics.

transverse and axial planes. The intrinsic resolution of the detectors is limited partly by the thickness of the crystal, which is needed for sensitivity, and partly by the short pulse-integration time, which is needed for high count rate capability. Research on improving the
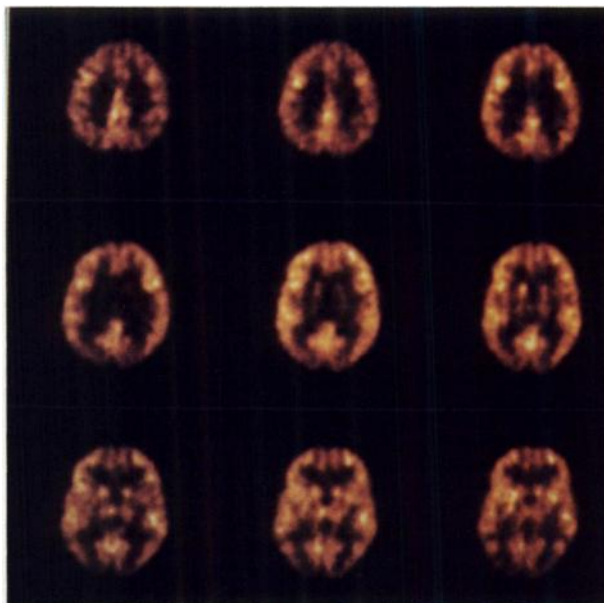
FIGURE 11
Transverse sections, 6 mm thick with 4 mm spacing, of [18F] FDG brain study. The patient was injected with 4.8 mCi and scanned for 50 min. Only nine representative sections are shown.
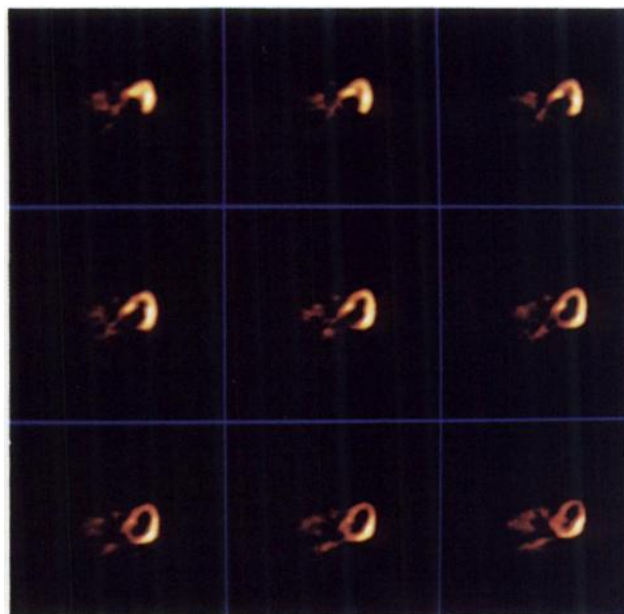
FIGURE 13
Transverse sections, 4 mm thick with 4 mm spacing, of [18F] FDG cardiac study. The patient was injected with 8 mCi and scanned for 12 min.

detector performance continues, including measuring the depth-of-interaction in the crystal to reduce the parallax error that occurs with oblique angles of incidence (24) and extending the ability to position events near the edges of the detector. The high count rate performance has been studied extensively, and requires using delay-line pulse clipping, a local centroid positioning algorithm, a short integration time, and an upper level energy discriminator. Pulse-by-pulse variable integration, to optimize the resolution for a range of countrates, has been investigated but not implemented.

The PENN-PET was designed without slice-defining septa and with a large axial acceptance angle to allow volume imaging. The large acceptance angle maximizes the sensitivity, but it adversely affects the spatial resolution at distances from the center of the scanner and increases the scatter fraction. The variation of the spatial resolution can be minimized by using a three-dimensional reconstruction algorithm, without affecting the sensitivity, or by limiting the axial acceptance angle and using a two-dimensional filtered backprojection technique. While research continues on implementing a three-dimensional algorithm, the constrained Fourier filtered backprojection technique is used for patient studies because of the time required to reconstruct three-dimensionally. The scatter fraction can be reduced by raising the lower level energy discriminator to the photopeak edge. In addition, more sophisticated techniques for scatter, random, deadtime, and attenuation corrections are under investigation.

In summary, the PENN-PET scanner is capable of brain and whole-body imaging, with a maximum 50-cm diameter transverse FOV and 9-cm axial FOV. A large number of static [^{18}F]FDG brain studies and some cardiac studies have been performed, in addition to brain blood flow studies and dynamic ^{18}F-n-methyl-spiperone neuroreceptor studies. The scanner has sufficient sensitivity and count rate capability to produce high quality volume images for most types of studies.

ACKNOWLEDGMENTS

REFERENCES

1. Muehllehner G, Karp JS. A positron camera using position-sensitive detectors: PENN-PET. *J Nucl Med* 1986, 27:90–98.
2. Hoffman EJ, Phelps ME, Huang SC, et al. Dynamic, gated and high resolution imaging with the ECAT III. *IEEE Trans Nucl Sci* 1986, NS-33:452–455.
3. Derenzo S, Huesman R, Cahoon J, et al. A positron tomo-graph with 600 BGO crystals and 2.6 mm resolution. *IEEE Trans Nucl Sci* 1988, NS-35:659–664.
4. Casey ME, Nutt R. A multicrystal two dimensional BGO detector system for positron emission tomography. *IEEE Trans Nucl Sci* 1986, NS-33:460–463.
5. Holte S, Eriksson L, Larsson J, et al. A preliminary evaluation of a positron camera system using weighted decoding of individual crystals. *IEEE Trans Nucl Sci* 1988; NS-35:730–734.
6. Karp JS, Muehllehner G, Beerbohm D, Mankoff D. Event localization in a continuous scintillation detector using digital processing. *IEEE Trans Nucl Sci* 1986, NS-35:550–555.
7. Karp JS, Mankoff DA, Muehllehner G. A position-sensitive detector for use in positron emission tomography. *Nucl Instr Meth* 1988, A273:891–897.
8. Mankoff D, Muehllehner G. Multi-frame data acquistion for PET-camera using an on-line microprocesor-based system. *IEEE Trans Nucl Sci* 1986, NS-33:443–445.
9. Karp JS, Muehllehner G. Performance of a position-sensitive scintillation detector. *Phys Med Bio* 1985, 30:643–655.
10. Mankoff DA, Muehllehner G, Karp JS. High countrate performance of a two-dimensionally position-sensitive detector for positron emission tomography. *Phys Med Bio* 1989, 34:437–456.
11. Seeger PA. A fast parallel encoding scheme for the Anger camera. *IEEE Trans Nucl Sci* 1984, NS-31:274–280.
12. Casey ME, Hoffman EJ. Quantitation in positron emission computed tomography: 7. A technique to reduce noise in accidental coincidence measurements and coincidence efficiency calibration. *J Compt Assist Tomogr* 1986, 10:845–850.
13. Daube-Witherspoon ME, Muehllehner G. Treatment of axial data in three-dimensional PET. *J Nucl Med* 1987, 28:1717–1724.
14. Daube-Witherspoon ME, Muehllehner G. An iterative image space reconstruction algorithm suitable for volume ECT. *IEEE Trans Med Imaging* 1986, MI-5:61–66.
15. Karp JS, Muehllehner G, Lewitt RM. Constrained Fourier space method for compensation of missing data in emission computed tomography. *IEEE Trans Med Imaging* 1988, MI-7:21–25.
16. Ollinger JM, Karp JS. An evaluation of three algorithms for reconstructing images from data with missing projections. *IEEE Trans Nucl Sci* 1988, 35:629–634.
17. Edholm PR, Lewitt RM, Lindholm B. Novel properties of the Fourier decomposition of the sinogram. *Proc Soc Photo-Opt Instrum Eng* 1986, 671:8–18.
18. Hoffman EJ, Digby WM, Germano G, Mazziotta JC, Huang SC, Phelps ME. Performance of a NeuroPet system employing 2-D modular detectors. *J Nucl Med* 1988, 29:983.
19. Mankoff D, Muehllehner G. Performance of positron imaging systems as a function of energy threshold and shielding depth. *IEEE Trans Med Imaging* 1984, MI-3:18–24.
20. Karp JS, Muehllehner G, Mankoff DA. The effect of axial acceptance angle and energy threshold on the performance of a PET tomograph. *J Nucl Med* 1989, 30:766.
21. Thompson CJ. The effect of collimation on scatter fraction in multi-slice PET. *IEEE Trans Nucl Sci* 1988, NS-35:598–602.
22. Stearns CW, Burnham CA, Chesler DA, Brownell GL. Simulation studies for cylindrical positron tomography. *IEEE Trans Nucl Sci* 1988, NS-35:708–711.
23. Mankoff DA, Muehllehner G, Karp JS. The effect of detector performance on high countrate PET imaging with a tomograph based on position-sensitive detectors. *IEEE Trans Nucl Sci* 1988, NS-35:592–597.
24. Karp JS, Daube-Witherspoon ME. Depth-of-interaction determination in NaI(Tl) and BGO scintillation crystals using a temperature gradient. *Nucl Instr Meth* 1987, A260:509–517.